Modelling and validation of magnetically suspended turbomolecular pump rotor considering blade structure

Song DING*, Jin ZHOU*, Yonghui WANG*, Yang ZHOU* and Yue ZHANG*
*College of Mechanical & Electrical Engineering, Nanjing University of Aeronautics and Astronautics
No. 29, Yudao Street, Nanjing, Jiangsu 210016, China
E-mail: 3445709461@qq.com

Abstract
The magnetically suspended turbomolecular pumps (MSTMPs) are critical for ultra-high vacuum generation, employing rotors with multistage flexible blades. In experimental and operational observations, the flexibility of these blades induces shaft-blade coupled bending vibrations that risk instability when coinciding with controller bandwidths. To accurately characterize these dynamics and enable vibration control strategies, a comprehensive numerical model is developed and experimentally validated. The effect of the bolted-joint interface contact between the turbo and shaft was modelled as uniformly distributed massless spring units, blade dynamics were discretized using plane beam elements incorporating centrifugal stiffening effects. The model is validated through modal tests and frequency response comparisons demonstrated accurate prediction of shaft-turbo bending modes and turbo-blade coupled modes with natural frequency errors ≤10%.

Keywords : Active Magnetic Bearing, Turbomolecular pump, Bolted joint, Blade Modelling, Dynamic Analysis

1. Introduction

Active magnetic bearings (AMBs) have been widely used in pumps and other turbomachinery applications (Schweitzer and Maslen, 2009). Magnetically suspended turbomolecular pumps (MSTMPs) provide ultra-high vacuum environments through high-speed rotation. Their rotor, featuring multistage flexible blades on a central shaft, experiences complex dynamics. While conventional research emphasizes rotor whirl and first bending modes (Zhang et al., 2024), experiments and simulations confirm blade flexibility induces critical shaft-blade coupled bending vibrations (She et al., 2018; Moreira and Thouverez, 2019a; Moreira and Thouverez, 2019b;). These modes arise from blade dynamic deformations under centrifugal and aerodynamic loads (Yao et al., 2024), readily excited at specific speeds (Moreira and Thouverez, 2019a; Zeng et al., 2025). If their frequencies overlap with the controller bandwidth, instability can occur (Moreira and Thouverez, 2019a). Critically, blade resonance amplitudes may exceed 20% of synchronous vibrations (Moreira and Thouverez, 2019a), posing significant safety risks. Therefore, accurate characterization of shaft-blade coupled dynamics is paramount for MSTMP stability.

Existing blade-rotor modeling approaches exhibit notable limitations (She and Li, 2022). Rigid rotor models (Wei et al., 2023) or simplified flexible models ignoring blade structure (Moreira and Thouverez, 2019a) fail to capture localized blade vibrations and coupling mechanisms. Transfer matrix methods, while computationally efficient, introduce >10% errors in critical frequencies due to oversimplified turbine geometry (Moreira and Thouverez, 2019a). Assumed-modes methods employing Rayleigh-Ritz formulation and Euler-Bernoulli beam theory (Moreira and Thouverez, 2019b) can model blade dynamics but rely on extensive modal coordinates, complicating controller synthesis and hindering real-time applications.

This study proposes a novel shaft-blade integrated modeling methodology for MSTMP rotors, utilizing the finite element energy method combined with Lagrange's equations:

(1) Bolted-joint interface modeling: The turbo-shaft interface contact is represented by uniformly distributed massless spring units, characterized by normal and tangential contact stiffness derived from a microscopic contact model

(2) Blade dynamics and model assembly: Blades are discretized using plane beam elements, explicitly incorporating centrifugal stiffening effects and coupled to the turbo structure via coordinate transformation matrices for eight circumferential blade groups. The shaft, turbo, and blade subsystem matrices are integrated through systematic finite

element assembly techniques.

The fidelity of the developed rotor model was rigorously validated through experimental modal testing under free-free boundary conditions. Furthermore, it provides an essential foundation for designing targeted active vibration control strategies, such as optimized notch filters, to suppress identified critical resonant modes and enhance MSTMP stability and safety.

2. Description of the system studied

The test rig employs an asymmetric rotor levitated by two identical radial AMBs and two axial AMBs, powered in differential driving mode with 8-pole configurations and 0.25 mm air gaps (Fig. 1). The rotor is driven by a permanent magnet synchronous motor, with its upper section mounting a multistage-turbine blade assembly and its lower section mounting a thrust disk serving as the active component for the axial AMBs. Components on the mid-shaft include laminated silicon steel sheets, a flux isolation ring, permanent magnets, and a motor sleeve. Each AMB is equipped with touch-down bearings (TDBs) featuring 0.125 mm air gaps and two non-colocalized eddy current sensors.

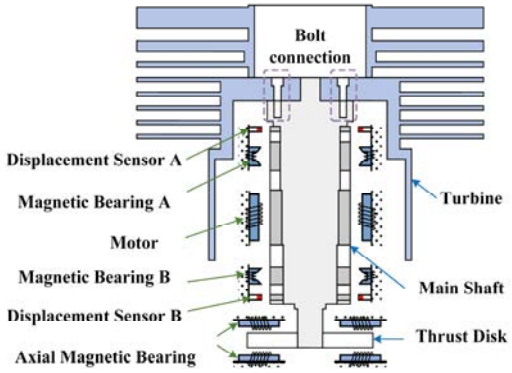

Fig. 1 Basic structure of a magnetic levitation turbomolecular pump.

3. Modelling of magnetically suspended turbomolecular pump rotor considering blade structure

The modelling of the magnetically suspended turbomolecular pump rotor consists of two parts: the model of shaft-turbo structure and the model of blade structure. These two models are combined by matrix assembly.

3.1 Modelling of shaft-turbo structure considering bolted joint

The schematic diagram of shaft-turbo structure is shown in Fig. 2. The bolted-joint interface contact between the turbo and the shaft is modelled as a uniform distribution of massless spring units across the contact area. The stiffness of these massless spring units is called contact stiffness, which is further differentiated into normal contact stiffness k_f and tangential contact stiffness k_q. The directions of k_f and k_q are aligned parallel to the normal contact force and tangential contact force on the contact interface, respectively. The values of k_f and k_q under different torques have been calculated based on the microscopic contact model and experimental identification in our previous research (Zhou et al., 2024). The outer radius of the contact area is denoted as the contact radius R_b and the inner radius of the contact area is denoted as R.

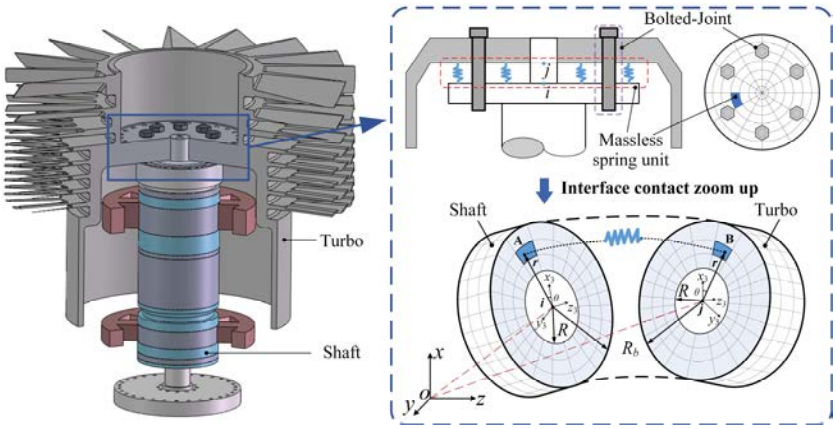

Fig. 2 Schematic diagram of the shaft-turbo structure considering bolted joint.

To build this shaft-turbo structure model, the finite element model of the shaft and turbo should be established firstly

as shown in Fig. 3. It can be seen that the shaft model consists of the beam element (which has 2 nodes and 8 DOFs) and rigid disk element (in terms of thrust disk and other fitting section on the shaft), the turbo is modelled based on the beam element. The shaft model and turbo element are connected by the spring element, which will be described in section 3.1. The modelling of the blade will be presented in section 3.2.

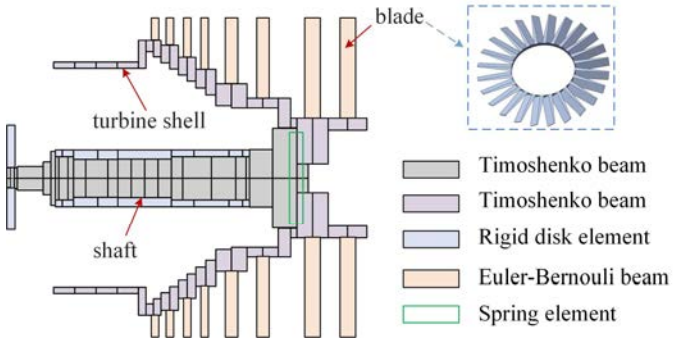

Fig. 3 Schematic diagram of finite elements of different sections.

The dynamic equations of the shaft and the turbo can be expressed as Eq. (1).

$$\begin{cases} \boldsymbol{M}_R\ddot{\boldsymbol{q}}_R + \left(\boldsymbol{C}_R + \Omega\boldsymbol{G}_R\right)\dot{\boldsymbol{q}}_R + \boldsymbol{K}_R\boldsymbol{q}_R = 0 \\ \boldsymbol{M}_T\ddot{\boldsymbol{q}}_T + \left(\boldsymbol{C}_T + \Omega\boldsymbol{G}_T\right)\dot{\boldsymbol{q}}_T + \boldsymbol{K}_T\boldsymbol{q}_T = 0 \end{cases} \tag{1}$$

where the $\boldsymbol{M}$, $\boldsymbol{C}$, $\boldsymbol{K}$, $\boldsymbol{G}$ are the mass, the damping, he stiffness and the gyroscopic matrices, respectively. Ω is the rotation speed of the shaft-turbo structure. $\boldsymbol{q}$ is the degrees of freedom. The subscript 'R' and 'T ' represent shaft and turbine respectively.

In the modeling of interface contact, the interface contact between the disk and the rotor is equivalent to spring units uniformly distributed over the contact interface, as shown in Fig. 2. The spring unit connects any point A (x_A, y_A, z_A) on the rotor con-tact interface and its corresponding point B (x_B, y_B, z_B) on the disk contact interface. There is relative deformation between the contact interfaces when the rotor vibrates. The energy generated by the spring deformation is calculated to study the influence of interface contact.

As shown in Fig. 2, floating coordinate O_i-$x_3y_3z_3$ and O_j-$x_3y_3z_3$ are established by taking the contact interface centers I and j as the coordinate origin and coordinate transformation in order to obtain the relative deformations of spring unit in x, y, z directions. The generalized coordinates of centers I and j are (x_i,y_i,α_i,β_i,z_i,ωt) and (x_j,y_j,α_j,β_j,z_j,ωt) in the absolute coordinate system O-xyz, where x_i, y_i, and z_i (x_j, y_j, and z_j) are the translations of I (j) in the x, y and z directions and α_i, β_i, and ωt (α_j, β_j, and ωt) are the rotations of I (j) around the x, y and z axis, x_3y_3 plane coincides with the contact interface and the orientation of z_3 is perpendicular to the contact surface. In a floating coordinate system, the coordinates of point A and B can be determined by the polar coordinates (r,θ), where r represents the distance between point A and center i or the distance between point B and center j, θ represents the angle between line Ai, Bj and x_3 axis, counterclockwise.

The total energy U generated by the spring unit is obtained by summing up the unit spring energy Δu as Eq. (2).

$$\begin{aligned} U &= \iint_S \frac{1}{2}\left(k_q\Delta x^2 + k_q\Delta y^2 + k_f\Delta z^2\right)\mathrm{d}S \\ &= 0.5k_q\iint_S \mathrm{d}S\left[\left(x_j - x_i\right)^2 + \left(y_j - y_i\right)^2\right] + 0.5k_f\iint_S y^2\mathrm{d}S\left(\alpha_j - \alpha_i\right)^2 + 0.5k_f\iint_S x^2\mathrm{d}S\left(\beta_j - \beta_i\right)^2 \end{aligned} \tag{2}$$

where Δx=x_B-x_A, Δy=y_B-y_A, Δz=z_B-z_A, S denotes the contact area. The total energy of the spring unit can be expressed as the elastic potential energy Eq. (3).

$$\begin{aligned} U &= \frac{1}{2}\begin{bmatrix} q_i & q_j \end{bmatrix}\boldsymbol{K}_{Eb}\begin{bmatrix} q_i & q_j \end{bmatrix}^T \\ \boldsymbol{K}_{Eb} &= \begin{bmatrix} diag\left(k_p,k_p,k_c,k_c\right) & -diag\left(k_p,k_p,k_c,k_c\right) \\ -diag\left(k_p,k_p,k_c,k_c\right) & diag\left(k_p,k_p,k_c,k_c\right) \end{bmatrix} \\ k_p &= k_q\pi\left(R^2 - R_b^2\right), \quad k_c = 0.25k_f\pi\left(R^4 - R_b^4\right) \end{aligned} \tag{3}$$

where $\boldsymbol{K}_{Eb}$ is the additional stiffness matrix generated by interface contact.

The dynamic equation of the shaft-turbo model can be expressed as Eq. (4) and the matrix assembly is shown in

$$\left(\boldsymbol{M}_R+\boldsymbol{M}_T\right)\ddot{\boldsymbol{q}}_r+\left(\boldsymbol{C}_R+\boldsymbol{C}_T\right)\dot{\boldsymbol{q}}_r+\left(\boldsymbol{K}_R+\boldsymbol{T}_e^{\mathrm{T}}\boldsymbol{K}_{Eb}\boldsymbol{T}_e+\boldsymbol{K}_T\right)\boldsymbol{q}_r=0 \tag{4}$$

where $\boldsymbol{q}_r$ is the degrees of freedom of the shaft-turbo structure.

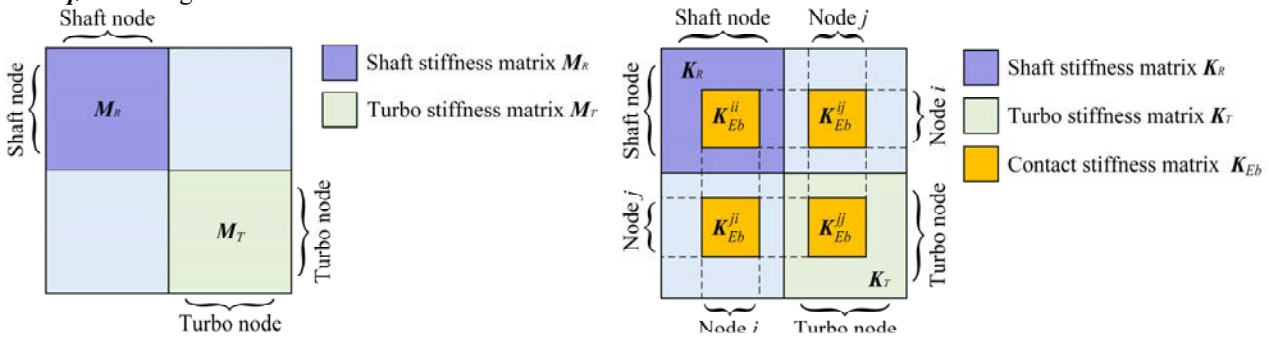

(a) Mass matrix assembly (b) Stiffness matrix assembly

Fig. 4 Schematic diagram of matrix assembly of shaft-turbo structure.

3.2 Modelling of blade structure and matrix assembly

The blade structure modelling and matrix assembly is described in this section and the schematic diagram of the blades is shown in Fig. 5. The blades on the turbo can be divided into eight groups and each group has its corresponding node on the turbo, each group consists of several blades.

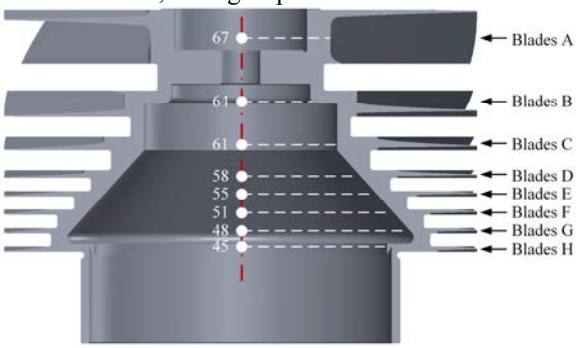

Fig. 5 Schematic diagram of blades and grouping.

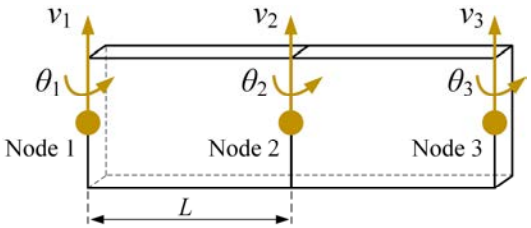

Fig. 6 Schematic diagram of plane beam element.

The blade is modelled based on plane beam element, as shown in Fig. 7. Each plane beam element has two nodes, each node has two DOFs (lateral displacement v and rotation θ). The generalized coordinate of each element can be expressed as $\boldsymbol{q}=[v_1, \theta_1, v_2, \theta_2, v_3, \theta_3]^{\mathrm{T}}$.

The mass matrix $\tilde{\boldsymbol{M}}$, stiffness matrix $\tilde{\boldsymbol{K}}$ and centrifugal stiffness matrix $\tilde{\boldsymbol{K}}c$ of each plane beam element can be expressed as Eq. (5)~(7), respectively.

$$\tilde{\boldsymbol{M}}=\frac{\rho AL}{420}\begin{bmatrix}156 & 22L & 54 & -13L\\ 22L & 4L^2 & 13L & -3L^2\\ 54 & 13L & 156 & -22L\\ -13L & -3L^2 & -22L & 4L^2\end{bmatrix},\quad \tilde{\boldsymbol{K}}=\frac{EI}{L^3}\begin{bmatrix}12 & 6L & -12 & 6L\\ 6L & 4L^2 & -6L & 2L^2\\ -12 & -6L & 12 & -6L\\ 6L & 2L^2 & -6L & 4L^2\end{bmatrix} \tag{5}$$

$$\tilde{\boldsymbol{K}}\boldsymbol{c} = \rho A\Omega^2 \begin{bmatrix} k_{11} & k_{12} & k_{13} & k_{14} \\ k_{12} & k_{22} & k_{23} & k_{24} \\ k_{13} & k_{23} & k_{33} & k_{34} \\ k_{14} & k_{24} & k_{34} & k_{44} \end{bmatrix}$$

$$k_{11} = \frac{6\alpha_0}{5L} + \frac{3\alpha_1}{5} + \frac{12L\alpha_2}{35},\quad k_{12} = \frac{\alpha_0}{10} + \frac{L\alpha_1}{10} + \frac{L^2\alpha_2}{14},\quad k_{13} = -\frac{6\alpha_0}{5l} - \frac{3\alpha_1}{5} - \frac{12L\alpha_2}{35} \tag{6}$$

$$k_{14} = \frac{\alpha_0}{10} - \frac{L^2\alpha_2}{35},\quad k_{22} = \frac{L(28\alpha_0 + 7L\alpha_1 + 4L^2\alpha_2)}{210},\quad k_{23} = -k_{12},\quad k_{24} = -\frac{L(14\alpha_0 + 7L\alpha_1 + 6L^2\alpha_2)}{420}$$

$$k_{33} = \frac{6\alpha_0}{5l} + \frac{12L\alpha_2}{35} + \frac{3\alpha_1}{5},\quad k_{34} = -k_{14},\quad k_{44} = \frac{L(28\alpha_0 + 21L\alpha_1 + 18L^2\alpha_2)}{210}$$

where ρ is the density of element， A is the cross-section area of element，L is the length of element，E is the Young's module of the element，I is the element's inertia moment of cross-section.

In Eq. (6), α_0, α_0 and α_0 can be expressed as

$$\begin{cases} \alpha_0 = -\dfrac{3L^2}{2} + 3L^2 i - \dfrac{3L^2 i^2}{2} - NL^2 + NiL^2 + \dfrac{N^2L^2}{2} + LR - iLR + NLR \\ \alpha_1 = 2L - 2iL - R \\ \alpha_2 = -\dfrac{1}{2} \end{cases} \tag{7}$$

where N is the number of elements in one blade (N=3), i means the i-th element (i=1, 2, 3).

Based on the plane beam element above, the blade is modelled as shown in Fig. 7. Taking Blades A group as example, the blades are denoted as: Blade A1, Blade A2,…,Blade An, each blade can be divided to three elements, the third node on the blade n in blades A group, the angle between X axis can be expressed as φ_{An}.

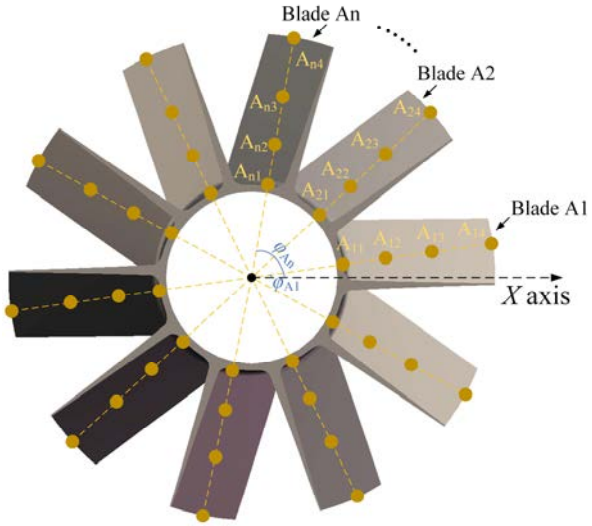

Fig. 7 Schematic diagram of blade node.

Taking Blade An as example, consists of four nodes and three elements. In order to let the v axis (blade structure) coincide with the x axis (turbo structure) and let the θ axis (blade structure) coincide with the α axis (turbo structure), the angle coordinate transformation matrix is introduced to the modelling as Eq. (8),

$$\boldsymbol{T}_{\mathrm{An}}=\begin{bmatrix}\cos(\varphi_{\mathrm{An}}) & \sin(\varphi_{\mathrm{An}}) & 0 & 0\\ -\sin(\varphi_{\mathrm{An}}) & \cos(\varphi_{\mathrm{An}}) & 0 & 0\\ 0 & 0 & \cos(\varphi_{\mathrm{An}}) & \sin(\varphi_{\mathrm{An}})\\ 0 & 0 & -\sin(\varphi_{\mathrm{An}}) & \cos(\varphi_{\mathrm{An}})\end{bmatrix} \tag{8}$$

After the angle coordinate transformation, the mass matrix, stiffness matrix and centrifugal stiffness matrix can be expressed as Eq. (9),

$$\begin{cases}\boldsymbol{M}=\boldsymbol{T}_{\mathrm{An}}{}^{\mathrm{T}}\cdot\tilde{\boldsymbol{M}}\cdot\boldsymbol{T}_{\mathrm{An}}\\ \boldsymbol{K}=\boldsymbol{T}_{\mathrm{An}}{}^{\mathrm{T}}\cdot\tilde{\boldsymbol{K}}\cdot\boldsymbol{T}_{\mathrm{An}}\\ \boldsymbol{Kc}=\boldsymbol{T}_{\mathrm{An}}{}^{\mathrm{T}}\cdot\tilde{\boldsymbol{Kc}}\cdot\boldsymbol{T}_{\mathrm{An}}\end{cases} \tag{9}$$

Finally, the matrix assembly of turbo matrix (mass matrix and stiffness matrix) and blade matrix (mass matrix, stiffness matrix and centrifugal stiffness matrix) is shown in Fig. 8. Since we take the Blades A as example, the shared node of turbo model and blade node is node 67 (as shown in Fig. 5). The mass matrix, stiffness matrix and centrifugal stiffness matrix of the blade are all connected to the mass matrix and stiffness matrix of turbo at the location of node 67.

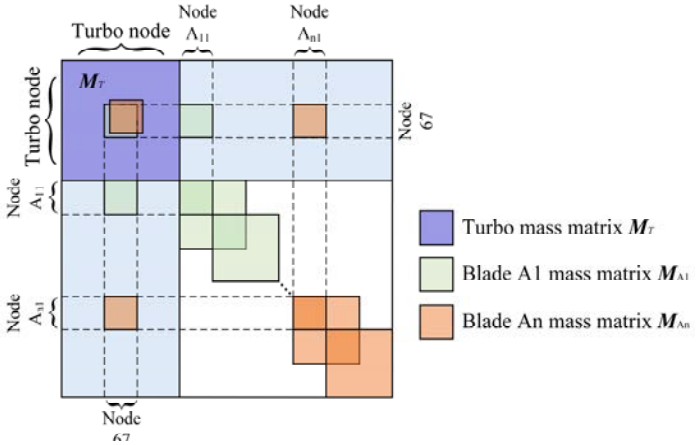

(a) Assembly of blade mass matrix

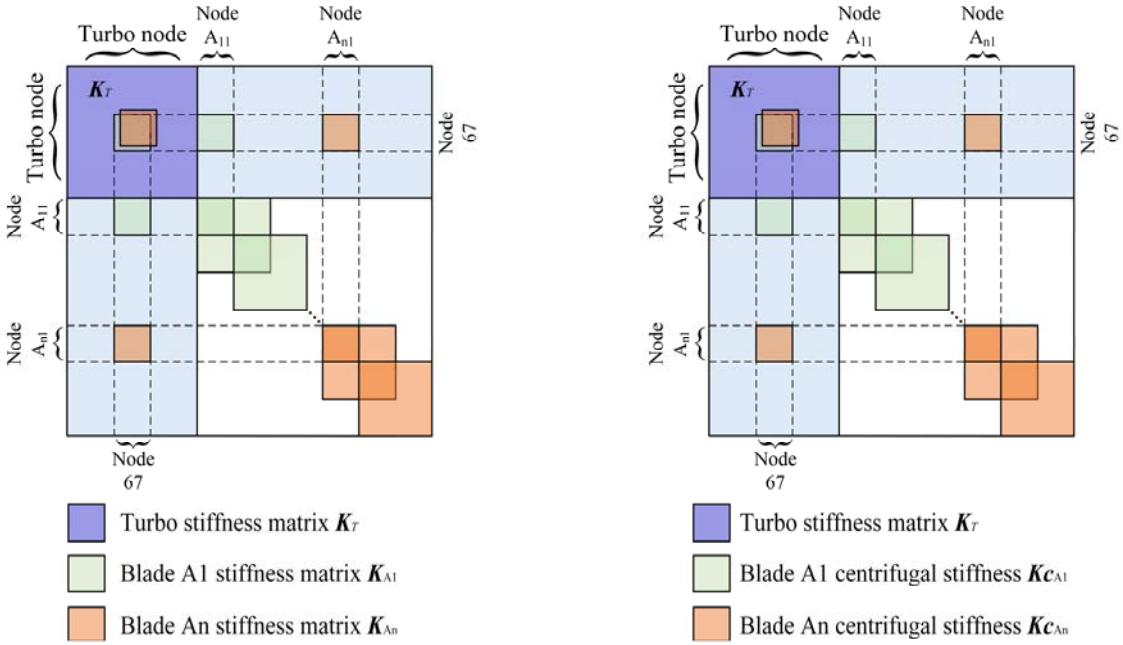

(b) Assembly of blade stiffness matrix (c) Assembly of blade centrifugal stiffness matrix

Fig. 8 Schematic diagram of matrix assembly of turbo-blade structure.

Based on the matrix assembly, the mass matrix $\boldsymbol{M}_{TB}$ and stiffness matrix $\boldsymbol{K}_{TB}$ of the turbo model with blade structure. To sum up, the dynamic equation of the shaft-turbo-blade structure can be expressed as,

$$\left(\boldsymbol{M}_R + \boldsymbol{M}_{TB}\right)\ddot{\boldsymbol{q}}_a + \left(\boldsymbol{C}_R + \boldsymbol{C}_T + \Omega\boldsymbol{G}_R + \Omega\boldsymbol{G}_T\right)\dot{\boldsymbol{q}}_a + \left(\boldsymbol{K}_R + \boldsymbol{T}_e^{\mathrm{T}}\boldsymbol{K}_{Eb}\boldsymbol{T}_e + \boldsymbol{K}_{TB}\right)\boldsymbol{q}_a = 0 \tag{10}$$

where $\boldsymbol{q}_a$ is the degrees of freedom of the shaft-turbo-blade structure.

4. Dynamic analysis and Experimental validation

In order to verify the accuracy of the rotor finite element model, the modal test is performed. As shown in Fig. 9, The rotor was suspended with the pneumatic tyre to simulate free-free state. An acceleration (PCB 352C65) was fixed on the laminations of AMB. The rotor was impacted at different position with an impact hammer (PCB 086C01). The measured forces and accelerations for each impact was then processed by using OROS-36 data acquisition and signal processing system. The sampling frequency was 51.2 kHz that cover largely the frequency band studied.

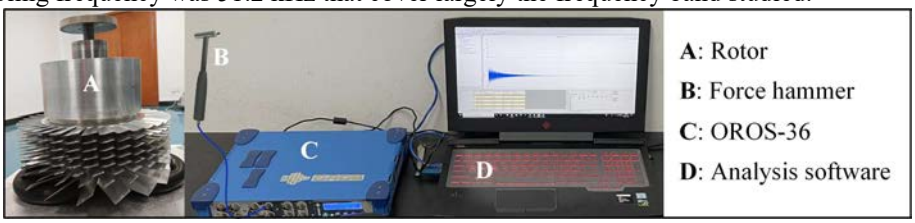

Fig. 9 The modal testing layout.

The frequency response function can be obtained by analyzing the rotor finite element model. The accuracy of the model can be verified by comparing the simulation results with the test results. The test result is shown in Fig. 10, there are six distinct peaks in the frequency range from 0 Hz to 1500 Hz. By analyzing the mode shapes of the shaft, f_1 is the mode formed by the relative motion between the shaft and the turbo, which is usually referred to as the first bending mode of rotor. f_6 is the mode dominate by thrust disk, not the coupling mode between the blade and the shaft. $f_2 \sim f_5$ is the mode formed by the coupling motion between the shaft and different layer of blades.

The proposed shaft-turbo-blade model can be used to predict the rotor-turbo coupling bending mode (f_1 and f_6) accurately, as shown in Fig. 10. For the mode ($f_2 \sim f_5$) formed by the coupling motion between the shaft and different layer of blades, the proposed shaft-turbo-blade model can be used to predict most of them. The accuracy of the model can be verified by comparing the simulation results with the test results.

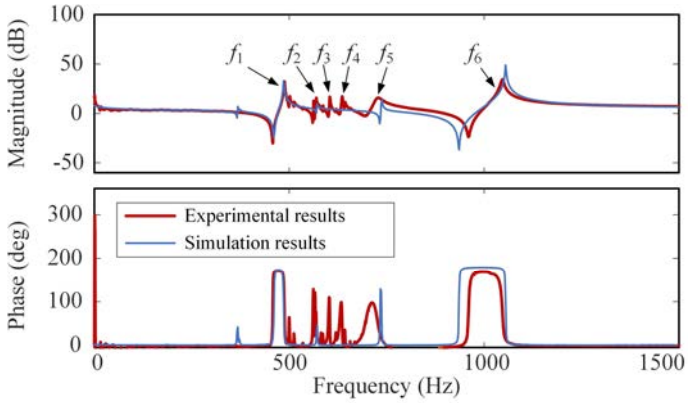

Fig. 10 The comparison of experimental and simulation frequency response

5. Conclusions

In this paper, a flexible rotor model considering the blade structure in the MSTMP is established based on the finite element method and the Lagrange equation, the accuracy of the rotor model is verified by using the modal test. The mechanism of the shaft-blade coupling mode and its influence on rotor vibration are revealed by combining the results of dynamic analysis and experimental validation. The rotor model established in this paper can be used to predict the modal characteristics, analyze the coupling mode vibration characteristics and design corresponding controller.

Acknowledgments and conflicts of interest

This work was supported by the National Natural Science Foundation of China (52475060).

The authors declare that they have no known competing financial interests or personal relationships that could have appeared to influence the work reported in this paper.

References

Moreira, A. B. B. and Thouverez, F., Dynamic modelling and vibration control of a turbomolecular pump with magnetic bearings in the presence of blade flexibility[M]// DI MAIO D. Rotating Machinery, Vibro-Acoustics & Laser Vibrometry, Volume 7. Cham: Springer, 2019a: 101–110. DOI:10.1007/978-3-319-74693-7_10.

Moreira, A. B. B. and Thouverez, F., Influence of blade flexibility on the dynamic response simulation of a turbomolecular pump on magnetic bearings[C]// Proceedings of the ASME Turbo Expo 2019: Turbomachinery Technical Conference and Exposition. Phoenix, Arizona, USA: ASME, 2019b: V07BT34A028. DOI:10.1115/GT2019-90990.

Schweitzer, G. and Maslen, E. H., Magnetic Bearings: Theory, Design, and Application to Rotating Machinery, Springer, Berlin, 2009.

She, H. and Li, C., "Analytical interpretation and numerical simulation on the dynamic coupling of a flexible cyclic blades-disk-shaft system", Applied Mathematical Modelling, 112: 726-748, 2022.

She, H., Li, C., Tang Q., et al., The investigation of the coupled vibration in a flexible-disk blades system considering the influence of shaft bending vibration[J]. Mechanical Systems and Signal Processing, 2018, 111: 545–569.

Wei, S., Zhou, J., Han, X. and Zheng, S., A simplified analysis method and suppression of the modalities of a magnetic levitation turbo rotor system, Vacuum, Vol. 217 (2023), p. 112452.

Yao, Y., Zhou, J., Ding, S., et al., Vibration suppression of magnetic levitation molecular pump rotor[J]. Journal of shock and vibration, 2024, 43(1): 116–122. DOI:10.13465/j.cnki.jvs.2024.01.014.

Zeng, K., Zhou, Y., Xu, Y. and Zhou, J., Modal vibration suppression for magnetically levitated rotor considering significant gyroscopic effects and interface contact, Actuators, Vol. 14, No. 2 (2025), p. 76.

Zhang, M., Tang, J., Zhou, J., et al., Vibration suppression of multi-stage-blade AMB-rotor using parallel adaptive and cascaded multi-frequency notch filters[J]. Applied Sciences, 2024, 14(14): 6255.

Zhou, Y., Zhou, J., Wang, Y., Zhang, Y., Xu, Y. and Lin, Z., Investigations on the modal vibration caused by bolted joint interface contact in the rotor-AMBs systems: Modelling and experimentation, Applied Mathematical Modelling, Vol. 134 (2024), pp. 249-267.